Hindawi Publishing Corporation
International Journal of Antennas and Propagation
Volume 2010, Article ID 850149, 8 pages
doi:10.1155/2010/850149

Research Article

Antenna Evaluation for Ultra-Wideband Microwave Imaging

Jeremie Bourqui, Mark A. Campbell, Trevor Williams, and Elise C. Fear

Department of Electrical and Computer Engineering, Schulich School of Engineering, University of Calgary, Calgary, AB, Canada T2N 1N4

Correspondence should be addressed to Elise C. Fear, fear@ucalgary.ca

Received 4 December 2009; Accepted 7 February 2010

Academic Editor: Miguel Ferrando

Numerous antenna designs have been proposed for microwave breast imaging utilizing an ultra-wideband frequency range. The antennas are typically compact, operate in an immersion medium, and have a band covering at least 2–10 GHz. We have developed 3 antennas for our UWB microwave breast imaging system. In this contribution, we compare the performance of the antennas in order to gain insight into the relationship between antenna performance metrics and image quality.

1. Introduction

Microwave techniques for breast imaging have recently generated a great deal of interest [1]. One group of approaches is termed radar-based imaging (e.g., [2–4]). This technique involves illuminating the breast with short-time, low-power pulses of microwave energy. Reflections from the breast are collected at the same or multiple antenna locations and are processed to create a three-dimensional image indicating the presence and location of tumors.

Radar-based microwave imaging requires the design of ultra-wideband (UWB) antennas that are suitable for near-field imaging and compatible with the particular system of interest. Several designs have been proposed and tested with prototype systems. For example, an array of low-profile, stacked patch antennas arranged on a hemisphere has been developed for a multistatic system at Bristol University [2]. A second example is an UWB pyramidal horn antenna developed at the University of Wisconsin for a monostatic system [4]. At the University of Calgary, we are developing a monostatic system, termed tissue sensing adaptive radar (TSAR) [3]. We have developed 3 candidate antennas, including a TEM horn antenna [5] and two versions of a balanced antipodal Vivaldi antenna (BAVA) [6]. One version of the BAVA antenna has a dielectric inclusion in the aperture in attempt to narrow the beam (BAVA-D) [7].

The three antennas are designed in order to meet criteria specific to an UWB, near-field imaging system, namely the TSAR prototype. For compatibility, the antenna must operate in an immersion medium of canola oil ($\varepsilon_r \approx 2.5$). This liquid is easy to implement, nontoxic, and provides a smaller antenna size, and reduced reflections from the skin when compared with free space. System dimensions require the antenna to fit inside a volume of approximately $10 \times 10 \times 10$ cm. The antenna is also required to have UWB performance. UWB performance is defined partly via the reflection coefficient, specifically $|S_{11}| < -10$ dB over a frequency range of 2–12 GHz. This bandwidth represents a tradeoff between resolution and tissue penetration. A second requirement related to UWB performance is the radiated field behavior. We require a close match between the radiated pulse and the derivative of the excitation signal, which is evaluated via fidelity. Finally, a directional radiation pattern is desired with a half-energy beam ranging from 3 to 8 cm at a distance of 2 cm from the aperture. Assuming 50% overlap between beams at neighboring antennas, this implies 8 to 20 antenna scan locations per row when considering scanning a 10 cm diameter object along a circular path with the antenna aperture located 2 cm from the object. While this is a practical number of antennas, tradeoffs between imaging capabilities and beam require investigation.

Although the three antenna designs meet the criteria outlined above, it is not clear how to select for TSAR

the most appropriate design for a given imaging scenario. This issue is investigated in this contribution. First, the three designs are reviewed in Section 2. Section 3 presents performance metrics and imaging results for the three antennas, including insight into tumor detection capabilities provided by different designs. Section 4 summarizes the work with conclusions.

2. TSAR Antenna Designs

The dimensions and construction of the three antennas are outlined in this section. All antennas are tested in a prototype system; an overview of the prototype and test objects is also provided.

2.1. BAVA. The BAVA antenna is it based on a standard balanced antipodal Vivaldi design; however, incorporates stacking substrate layers to balance the dielectric loading between the central and external metallization layers [6]. This additional feature also improves the efficiency since it isolates the metallization from the lossy canola oil. Figure 1 shows a layout diagram of the antenna. Dimensions are selected via simulations of various design choices and analysis of antenna behavior using finite difference time domain (FDTD) software (SEMCAD, SPEAG, Zurich). Detailed dimensions are provided in [6], and the overall size of the structure is 44 mm wide by 80 mm long by 12 mm thick (excluding the SMA connector).

The metallization layers are patterned using a lithography process. The layers are assembled by milling the appropriate shapes and bonding the layers. The substrate used is RT/Duroid 6002 (Rogers Corp.), which has a relative permittivity of 2.94. After bonding, the conductors are no longer visible. The completed antenna is shown in Figure 2.

2.2. BAVA-D. The BAVA-D is similar to the BAVA; however, includes a specially shaped piece of dielectric with higher permittivity in the antenna throat (Figure 3) [7]. The shape of the director is designed to avoid reflections from its extremities, that is, the start and the end of the aperture, shown, respectively, as A and B in Figure 3. Section A approximately follows the aperture curves while Section B has been limited to a simple triangle that reasonably reduces reflections from the aperture. The dimensions of the antenna and director are given in [7]. The substrate length is extended by 4 mm compared to the original design to accommodate the director placement; otherwise the overall size is the same as for the BAVA antenna. The director has two effects on antenna behavior. First, most of the energy is directed towards the aperture center. The second effect is related to the phase velocity, which will be lower in the director structure compared to the rest of the substrate. This produces differences in the propagation velocities between the director and the copper edges. As waves travel faster along the edges and the path length is physically longer, the overall effect is a phase front with enhanced planar characteristics near the aperture of the antenna (compared to the BAVA).

The BAVA-D is manufactured in a similar manner to the BAVA. The opening for the director is machined and the director is simply pressed into place.

2.3. TEM. The TEM horn antenna [5] is shown in Figure 4 and consists of a microstrip-to-parallel strip balun [8] attached to flared plates. The shape and separation of the plates vary to provide a transition from 50 ohm to 115 ohm impedance. Specifically, a linear variation in impedance along the antenna length is combined with an exponential variation in separation between the plates. The plate width at specific locations along the antenna length is calculated to provide the desired impedance. Dimensions and design parameters are obtained by performing parametric studies with simulation software (FEKO, EM Software and Systems, Stellenbosch). The final dimensions are provided in [5], and the overall dimensions of the antenna with balun are 80 mm $\times$ 50 mm $\times$ 50 mm, as shown in Figure 4.

The TEM horn antenna is implemented using acrylic structures to support the plates and sandwich the balun. The implemented design is shown in Figure 5. The white cap is an oil-proofing device to prevent leakage of canola oil into the cables.

2.4. Testing. In order to compare the performances of the three antennas, several experimental setups are utilized. To obtain the scattering parameters, one or two antennas of each design are immersed in a tank of canola oil ($\varepsilon_r = 2.5, \sigma = 0.04$ S/m). The antennas are attached to coaxial cables, and a vector network analyzer (8719ES, Agilent Technologies, Palo Alto, CA) is used to collect measurements.

To obtain the tumor response, a phantom tumor is inserted into the tank. The tumor consists of an epoxy with properties $\varepsilon_r = 10, \sigma = 0.01$ S/m (Eccostock HiK Cement, Randolph, MA). It is cylindrical in shape with 7.5 mm length and 9 mm diameter and attached to the end of a Plexiglas rod to aid in positioning. Reflections are recorded with the tumor and rod as well as with only a Plexiglas rod present. The two sets of reflections are subtracted in order to remove reflections from the antenna structure and rod.

To gain insight into imaging capabilities, a simple breast phantom is imaged in a prototype TSAR scanner. The prototype is shown in Figure 6, and consists of a tank of canola oil in which a positioning arm is located. The antenna is attached to the positioning arm, which scans vertically. The entire tank rotates in order to scan the antennas around the phantom. The breast phantom is positioned through a hole located in a plate placed on top of the tank.

The phantom is shown in Figure 7 and is made of a solid dielectric material with relative permittivity of 15 and loss tangent less than 0.002 (Eccostock HiK, Emerson and Cuming Microwave Products). The cylindrical component has diameter of 100 mm and extends 28.6 mm into the tank. A hemisphere with radius of 5 cm is joined to the cylinder. The bottom of the hemisphere is shaped to represent the nipple. It has a radius of 5.2 mm and is surrounded by a ring with diameter of 20 mm and thickness of 2 mm. A Teflon rod of diameter 7.9 mm and length 9.7 mm is placed in the breast

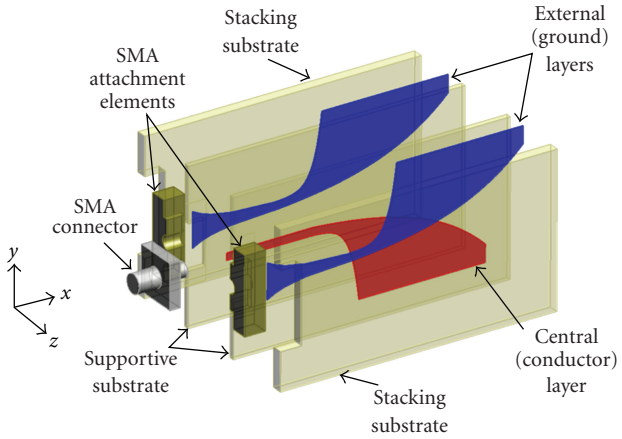

Figure 1: Exploded view of the BAVA antenna.

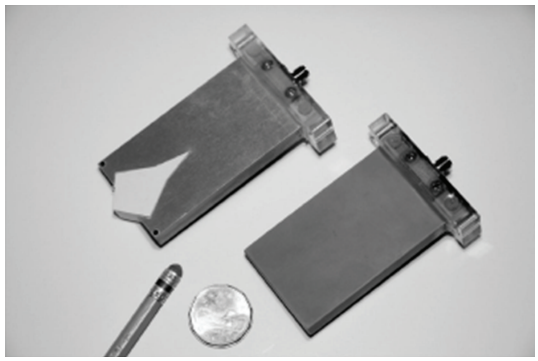

Figure 2: Implemented BAVA-D and BAVA antennas.

model. We define a coordinate system with the z-axis in the vertical direction, $z = 0$ at the top of the tank, and z decreasing towards the bottom of the tank. The inclusion is located at $x = 105.1$ mm, $y = 80.1$ mm, and $z = -49.7$ mm, corresponding to a radial distance of 25 mm from the center of the model. The Teflon rod has a relative permittivity of 2.1 and a conductivity of 0.0004 S/m. The electrical properties of the breast model and its inclusion differ from actual biological tissues; however, provide predictable geometry and electrical properties. These are key for comparison of antenna designs.

3. Antenna Performance

In order to assess the antenna performance, we examine S_{11}, fidelity, near-field beamwidth, and reflections from objects placed near the antenna. We also compare images of a breast phantom created with data collected by the different antennas.

3.1. Reflection and Transmission Coefficients. The reflection coefficients for the three designs are obtained by placing the antennas in a tank of canola oil and measuring S_{11}. Figure 8 compares the results, indicating that all antennas operate over extremely wide bands. The TEM antenna has a slightly

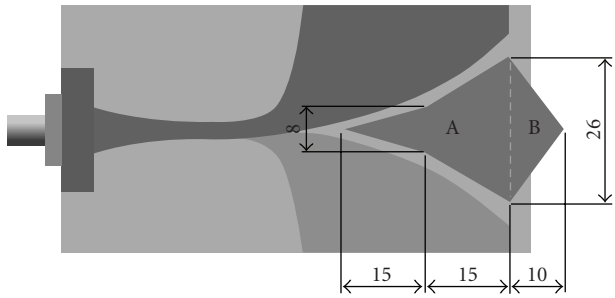

Figure 3: BAVA-D with shape and dimensions of director. The director is made of a dielectric with relative permittivity of 6.

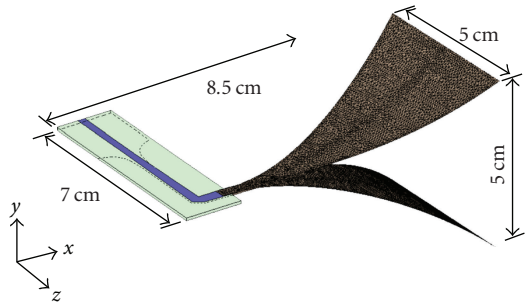

Figure 4: TEM horn antenna with balun.

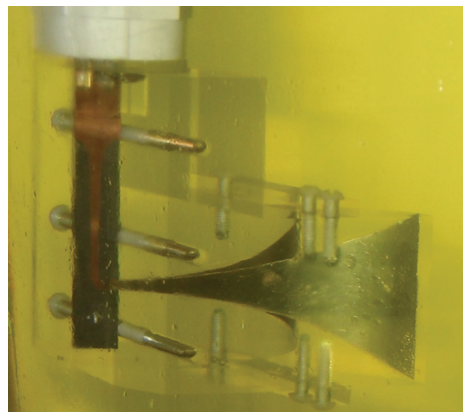

Figure 5: Implemented TEM horn.

Figure 6: TSAR prototype.

Figure 7: Dielectric breast phantom.

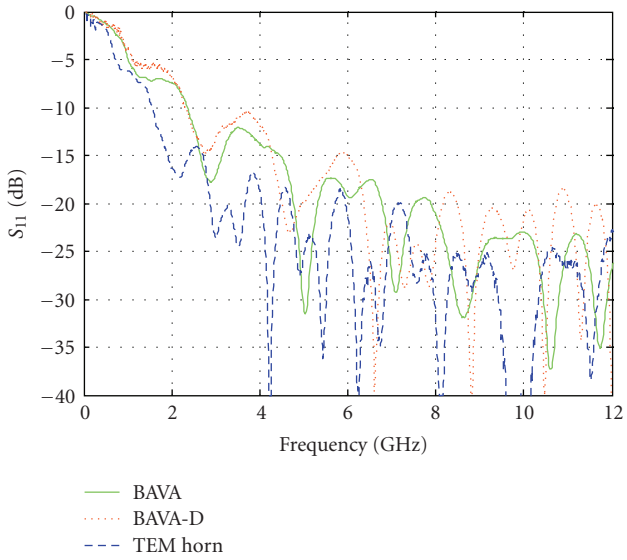

Figure 8: Measured S_{11} for all 3 antennas.

wider band, as the reflection coefficient reaches −10 dB at a lower frequency than the other antennas.

The transmission coefficient (S_{21}) is recorded with the antennas separated by 10 cm and the apertures aligned. Consistent with the S_{11} results, the TEM horn exhibits greater S_{21} than the other 2 designs at lower frequencies; however the transmission decreases above 4 GHz. The BAVA-D shows the strongest transmission at higher frequencies, consistent with the presence of the director to focus the beam of the antenna.

3.2. Radiated Fields. The near-field radiation performance is assessed by examining simulations of fidelity as well as the near-field beamwidth. A differentiated Gaussian signal is used as an excitation [3] and is given by

$$V(t) = V_0 * (t - t_0) * e^{-(t-t_0)/\tau^2}, \quad (1)$$

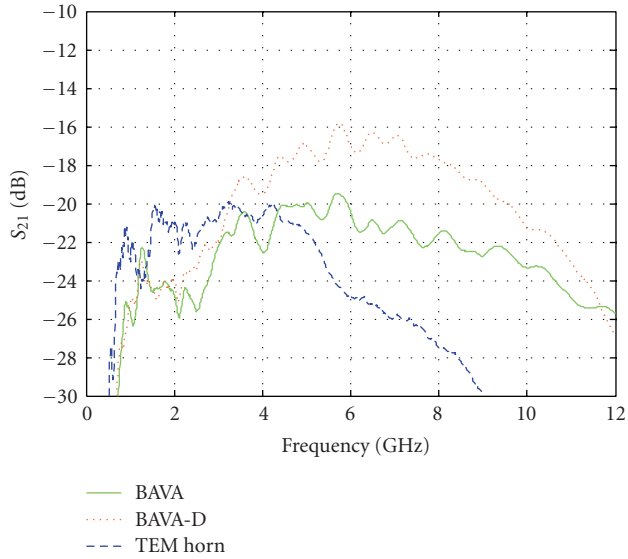

Figure 9: Measured S_{21} for all 3 antennas.

Table 1: Antenna performance 2 cm from aperture. The maximum fidelity value is provided.

Antenna	Fidelity	Beamwidth (mm)	
		Y	Z
BAVA	0.96	45	34
BAVA-D	0.99	42	23
TEM	0.93	47	58

where V_0 is used to adjust the amplitude of the pulse, τ = 62.5 ps and $t_0 = 4\tau$. The fidelity indicates the similarity between the radiated field and a reference signal, in this case the derivative of the excitation [9]. The near-field beamwidth is calculated by examining fields on selected planes. The energy density or energy flux density is computed, and values greater than half of the maximum are identified. The beamwidths are defined in the y and z directions using the values identified in the previous step. For scanning, all antennas are oriented with the y-dimension horizontal and the z-dimension vertical. Table 1 summarizes beamwidth and fidelity results.

All antennas have relatively good fidelity at 2 cm from the antenna aperture. All antennas have similar beamwidth in the y plane, which is the plane in which the antenna is scanned around the object. The beamwidth of the 3 antennas differs significantly in the z-direction (i.e., along the axis of the object of interest when positioned in the scanner).

3.3. Single Tumor Reflections. Reflections from objects representing tumors are observed. Measurements are collected in the frequency domain, and then signals are weighted with the pulse described by (1) and converted to the time domain. For a tumor located at 4 cm from the aperture, measured reflections are shown in Figures 10 and 11. Time domain reflections indicate that the BAVA-D provides the strongest tumor reflection, while the TEM horn provides

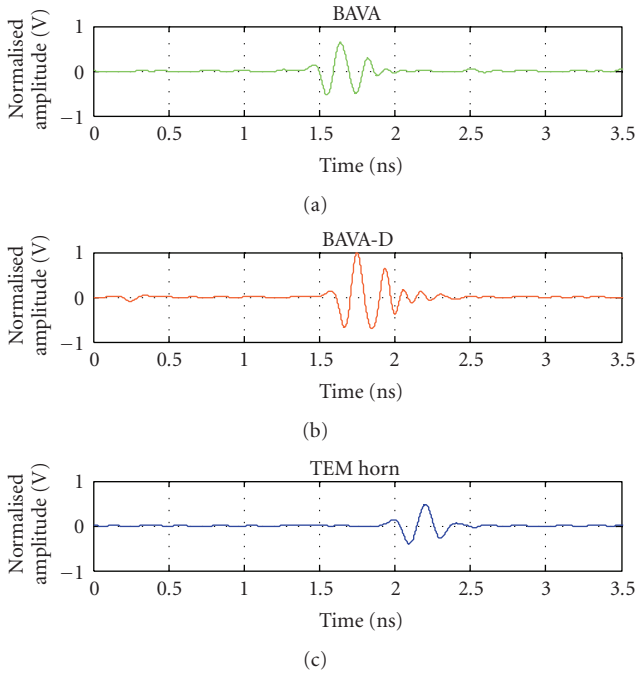

Figure 10: Normalized time-domain reflections from tumors recorded with each of the three antennas.

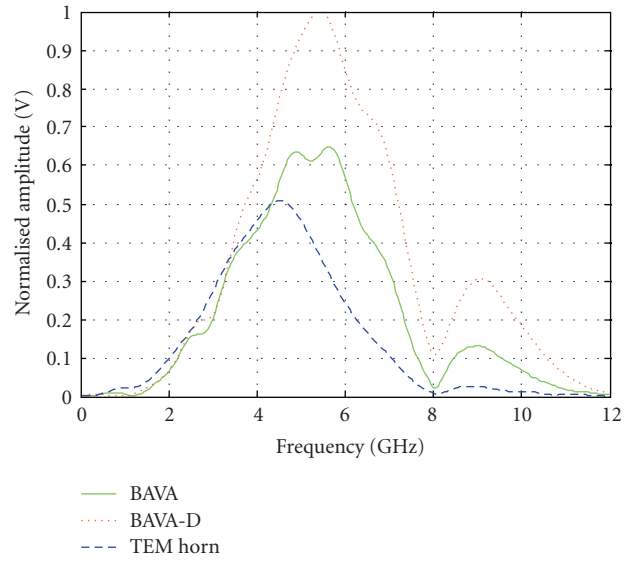

Figure 11: Frequency domain reflections from tumor recorded with each of the three antennas.

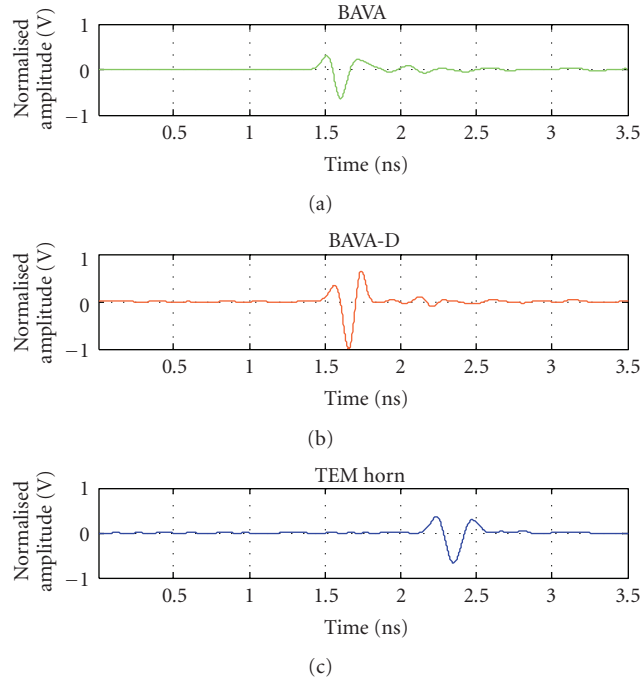

Figure 12: Single signal recorded from breast phantom with antennas approximately aligned with tumor. All signals are normalized to the maximum amplitude of the BAVA-D response.

the reflection with the least ringing. It can also be noted that the reflection appears later in time due to a greater electrical length of the TEM horn. Increased ringing after the main tumor response is noted when comparing the BAVA-D with the BAVA. Frequency-domain reflections presented in Figure 11 demonstrate slightly greater lower frequency content of the signal recorded with the TEM horn as well as increased sensitivity to higher frequencies with the BAVA and BAVA-D. These observations are consistent with Figure 9.

Figure 12 compares reflections from the phantom collected with each of the three antennas at $z = -48$ mm from a location approximately aligned with the inclusion. The center of the inclusion is 65.1 mm from the tip of the BAVA antennas and 65.5 mm from the tip of the TEM horn. Figure 12 shows that differences in the reflected waveforms exist between the antennas. The TEM horn again exhibits longer electrical length relative to the BAVA designs, resulting in a response that is received later in time. The large initial reflection is created from the interface between oil and the phantom material. Reflections from the inclusion (which should appear 0.65 nanosecond after the initial reflection) are not readily apparent. Therefore, the dominant response from the oil/phantom interface is removed using the RLS skin subtraction process outlined in [3] prior to further processing (with the specification that the skin is 0 mm thick).

3.4. Scanning. The BAVA, BAVA-D, and TEM antennas are attached to the TSAR prototype in turn and used to scan the breast phantom. For all antennas, the breast phantom and antenna aperture are separated by a minimum of 30 mm. The antenna is scanned to up to 7 rows (elevations) separated by 1 cm. In each row, the antenna is scanned around the phantom and measurements are taken at 20 locations per row. Rows are rotationally offset by 6 degrees in order to provide offset between measurement locations in neighboring rows.

Figures 13 and 14 compare focused images resulting from data collected with all three antennas. The size of the TEM horn in the vertical plane restricted the data collection close

to the top of the cylinder. Therefore, only 5 rows of data are collected with the TEM horn. For 5 rows, the antenna is scanned from $z = -88$ mm to $z = -48$ mm in 10 mm increments. Measurements are obtained at 20 locations per elevation (row), resulting in 100 scan locations. For a more effective comparison, the images in Figures 13 and 14 are reconstructed with data collected at the same 5 rows for all antennas. The surface of the model is determined using a laser sensor as reported in [10]. After reduction of the dominant reflection, the data are focused with a simple time-shift and sum algorithm [3]. The imaging volume is defined by the surface estimate; the surface estimate is also used to define the path lengths in oil and phantom material during travel time calculations.

Figures 13 and 14 indicate that the inclusion is detected with all 3 antennas. Figure 13 shows the cross-sectional images through the maximum tumor responses, indicating that the TEM horn antenna provides the most compact response. This is consistent with observations of reflections from single tumor models, as the TEM antenna exhibited the response with the least ringing. Figure 14 shows images on a plane passing through the axis of the phantom and the maximum tumor response. The TEM horn creates a response with larger physical extent than the BAVA antennas, while the BAVA-D creates the response with the smallest physical extent. This is consistent with the antenna beamwidths. Finally, the tumor responses are not detected at the true location but shifted toward the nipple region. This reflects the fact that the 5 rows of data are not collected symmetrically about the tumor location. Specifically, the errors in the x-y plane are approximately 2.5 mm (TEM), 2.5 mm (BAVA), and 1.4 mm (BAVA-D). In the z-direction, the tumor responses are translated by 9.3 mm, 9.3 mm, and 6.3 mm for the TEM, BAVA, and BAVA-D antennas, respectively. The BAVA-D response is closest to the known location, suggesting benefits for tumor response localization in practical scenarios when the scan pattern is not centered on the tumor location.

Next, images are created with the BAVA-D and BAVA antennas scanned to 7 rows (ranging from -88 mm to -28 mm and positioned symmetrically about the inclusion). The antennas scan closer to the top of the model due to the smaller vertical profile (compared to the TEM horn). Figure 15 shows the improvements with the inclusion of additional data. Specifically, the maximum responses are 9 mm and 3 mm closer to the known inclusion location in the z-direction with the BAVA and BAVA-D, respectively. Figure 15 also shows that the image created with the BAVA-D data exhibits a more localized tumor response.

Finally, we examine the relation between detection and scan pattern with the BAVA-D antenna. Images are reconstructed with different numbers of antenna locations, and the signal-to-clutter ratio (SCR) is noted in Table 2. The SCR relates the maximum of the focused tumor response to the maximum response in the image outside of the tumor response. To calculate this second response, the same three-dimensional area is zeroed for each dataset. We note that the center of the highest response is consistent for all of the scans considered in Table 2.

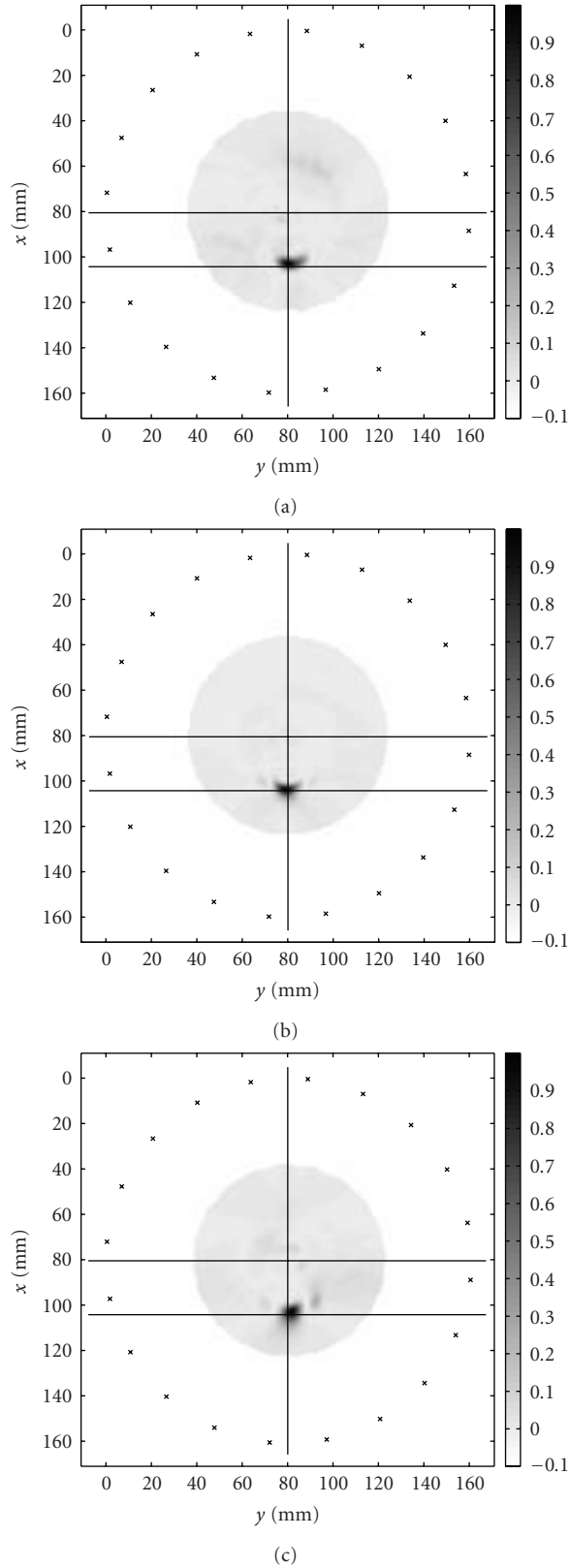

Figure 13: Comparison of focused tumor response between BAVA (a), BAVA-D (b), and TEM horn (c). The upper horizontal line shows the center of the phantom, while the lower shows the expected inclusion location along the x-axis. The vertical line shows the expected inclusion location along the y-axis. Each image is normalized to the specific dataset.

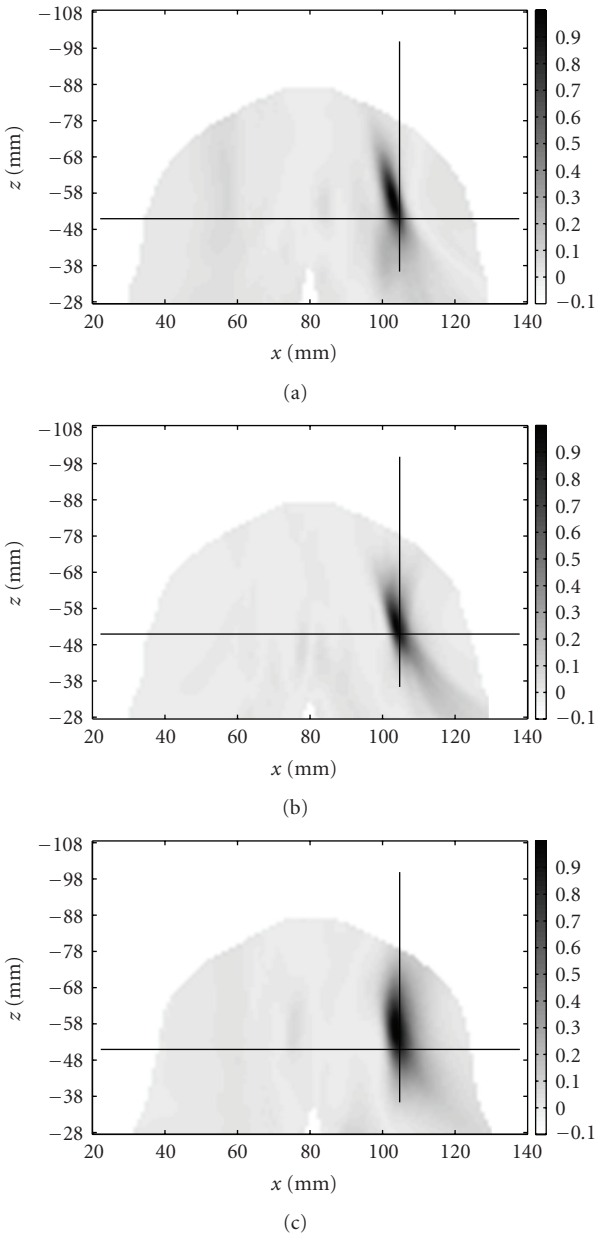

Figure 14: Comparison of focused tumor response between BAVA (a), BAVA-D (b), and TEM horn (c). The intersection of the thin lines shows the center of the inclusion. Each image is normalized to the specific dataset.

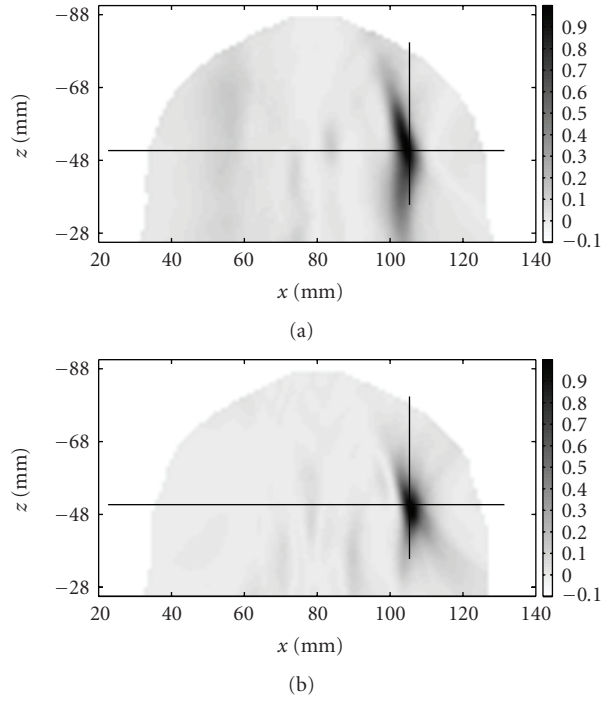

Figure 15: Comparison of focused tumor response between the BAVA (a) and BAVA-D (b) with 2 additional rows of data compared to Figure 13. The intersection of the thin lines indicates the location of the center of the inclusion. Each image is normalized to the specific dataset.

Table 2: Comparison of SCR for different scan densities.

Scan pattern	Signal-to-clutter (dB)
20 Ant/Row, 7 Rows	20.89
20 Ant/Row, 4 Rows	19.34
10 Ant/Row, 7 Rows	18.47
10 Ant/Row, 4 Rows	16.13
20 Ant/Row, 1 Row	10.87
10 Ant/Row, 1 Row	3.43
5 Ant/Row, 1 Row	0

Six different scan scenarios are summarized in Table 2. The SCR of the original scan (7 rows separated by 1 cm and 20 locations per row) indicates that the tumor is easily detected. By reducing the number of rows (omitting rows 2, 4, and 6), the SCR remains almost the same, suggesting that sufficient overlap between neighboring antenna beams is maintained. Fewer antennas per row result in a small reduction in SCR; however the inclusion is still easily detected. This suggests that approximately 50% overlap between neighboring antenna beams provides effective detection of inclusions in simple models. We anticipate benefits to increased scan pattern density with more complex models or realistic scenarios (i.e., increased clutter due to variations in dielectric properties of the breast interior). Finally, images are created with 1 row of antennas. When comparing a single row of 20 antennas with a full scan, the inclusion is still easily detected. We note that multiple rows do provide benefits in terms of localizing the tumor response along the z-axis. Detection becomes increasingly challenging with 10 antennas in a single row and is not possible with 5 antennas in a row. This reflects the limited overlap of the beams of the neighboring antennas. Overall, these results suggest the utility of the antenna beam in design of data collection strategies.

4. Conclusion

In this paper, we compare 3 candidate antennas for UWB near-field microwave imaging. The 3 designs have similar performance; however, exhibit different beamwidths in the z-direction. A TEM horn provides the best performance at lower frequencies; however it has the largest physical cross-section. This limits the physical range over which data may be easily acquired with a cylindrical scan pattern. The TEM horn also has the largest beamwidth in the z-direction, resulting in the least compact responses in the z-direction for a given scan pattern when compared with the other antennas. The BAVA antennas are more sensitive at the higher-frequencies and this sensitivity is expected to be beneficial for the breast imaging application, as tissue loss increases with frequency. The BAVA-D produces better localization of the inclusion response than the BAVA for a similar scan pattern. When combined with the improved higher frequency response, this suggests that the BAVA-D antenna is the best of the 3 candidates. Finally, inclusion detection is successful with an overlap of 50% of the beams of neighboring antennas (when considering patterns at 2 cm from the aperture). This suggests that the beamwidth may be used to design effective scan patterns. We note that the phantom analyzed in this paper does not contain inclusions other than the target, and an increased density of scan pattern may be required for UWB near-field imaging of more complex objects.

References

[1] E. C. Fear, "Microwave imaging of the breast," *Technology in Cancer Research and Treatment*, vol. 4, no. 1, pp. 69–82, 2005.

[2] M. Klemm, I. J. Craddock, J. A. Leendertz, A. Preece, and R. Benjamin, "Radar-based breast cancer detection using a hemispherical antenna array—experimental results," *IEEE Transactions on Antennas and Propagation*, vol. 57, no. 6, pp. 1692–1704, 2009.

[3] J. M. Sill and E. C. Fear, "Tissue sensing adaptive radar for breast cancer detection—experimental investigation of simple tumor models," *IEEE Transactions on Microwave Theory and Techniques*, vol. 53, no. 11, pp. 3312–3319, 2005.

[4] X. Li, E. J. Bond, B. D. van Veen, and S. C. Hagness, "An overview of ultra-wideband microwave imaging via space-time beamforming for early-stage breast-cancer detection," *IEEE Antennas and Propagation Magazine*, vol. 47, no. 1, pp. 19–34, 2005.

[5] M. A. Campbell, M. Okoniewski, and E. C. Fear, "TEM horn antenna for near-field microwave imaging," *Microwave and Optical Technology Letters*, vol. 52, no. 5, pp. 1164–1170, 2010.

[6] J. Bourqui, M. Okoniewski, and E. C. Fear, "Balanced antipodal Vivaldi antenna for breast cancer detection," in *Proceedings of the 2nd European Conference on Antennas and Propagation (EuCAP '07)*, pp. 1–4, Edinburgh, UK, November 2007.

[7] J. Bourqui, et al., "Balanced antipodal Vivaldi antenna with dielectric director for near-field microwave imaging," to appear in *IEEE Transactions on Antennas and Propagation*.

[8] M. A. Campbell, M. Okoniewski, and E. C. Fear, "Ultra-wideband microstrip to parallel strip balun with constant characteristic impedance," in *Proceedings of the EMTS International URSI Commission B. Electromagnetic Theory Symposium*, pp. 1–4, July 2007.

[9] T. P. Montoya and G. S. Smith, "A study of pulse radiation from several broad-band loaded monopoles," *IEEE Transactions on Antennas and Propagation*, vol. 44, no. 8, pp. 1172–1182, 1996.

[10] T. Cameron, T. C. Williams, J. Bourqui, M. Okoniewski, and E. C. Fear, "Comparison of microwave and laser surface detection for microwave imaging systems," in *Proceedings of the 13th International Symposium on Antenna Technology and Applied Electromagnetics and the Canadian Radio Sciences Meeting (ANTEM/URSI '09)*, pp. 1–4, Banff, Canada, 2009.